Edge localized mode rotation and the nonlinear dynamics of filaments

J. A. Morales, M. Bécoulet, X. Garbet, F. Orain, G. Dif-Pradalier, M. Hoelzl, S. Pamela, G. T. A. Huijsmans, P. Cahyna, A. Fil, E. Nardon, C. Passeron, and G. Latu

Citation: Physics of Plasmas **23**, 042513 (2016); doi: 10.1063/1.4947201
View online: http://dx.doi.org/10.1063/1.4947201
View Table of Contents: http://scitation.aip.org/content/aip/journal/pop/23/4?ver=pdfcov
Published by the AIP Publishing

Edge localized mode rotation and the nonlinear dynamics of filaments

J. A. Morales,[1] M. Bécoulet,[1] X. Garbet,[1] F. Orain,[2] G. Dif-Pradalier,[1] M. Hoelzl,[2] S. Pamela,[3] G. T. A. Huijsmans,[1] P. Cahyna,[4] A. Fil,[1] E. Nardon,[1] C. Passeron,[1] and G. Latu[1]
[1]*CEA, IRFM, 13108 St. Paul-Lez-Durance, France*
[2]*Max Planck Institute for Plasma Physics, Boltzmannstr. 2, 85748 Garching, Germany*
[3]*CCFE, Culham Science Centre, Abingdon, Oxon OX14 3DB, United Kingdom*
[4]*Institute of Plasma Physics ASCR, Za Slovankou 1782/3, 182 00 Prague 8, Czech Republic*

(Received 8 December 2015; accepted 15 March 2016; published online 26 April 2016)

Edge Localized Modes (ELMs) rotating precursors were reported few milliseconds before an ELM crash in several tokamak experiments. Also, the reversal of the filaments rotation at the ELM crash is commonly observed. In this article, we present a mathematical model that reproduces the rotation of the ELM precursors as well as the reversal of the filaments rotation at the ELM crash. Linear ballooning theory is used to establish a formula estimating the rotation velocity of ELM precursors. The linear study together with nonlinear magnetohydrodynamic simulations give an explanation to the rotations observed experimentally. Unstable ballooning modes, localized at the pedestal, grow and rotate in the electron diamagnetic direction in the laboratory reference frame. Approaching the ELM crash, this rotation decreases corresponding to the moment when the magnetic reconnection occurs. During the highly nonlinear ELM crash, the ELM filaments are cut from the main plasma due to the strong sheared mean flow that is nonlinearly generated via the Maxwell stress tensor. [http://dx.doi.org/10.1063/1.4947201]

I. INTRODUCTION

Edge Localized Modes (ELMs) are magnetohydrodynamic (MHD) instabilities that appear at the edge of the tokamak plasma in high confinement mode (H-mode). They are characterized by periodic bursts of matter and energy. The crash of this instability leads to the relaxation of the edge pressure pedestal, then the edge pedestal rebuilds and another ELM cycle occurs. The quantity of energy that is expelled periodically can cause partial erosion or melting of plasma-facing components. This could limit the operational capabilities of future larger tokamak devices like ITER and DEMO. For recent review articles on ELMs, we refer to Refs. 1 and 2.

In recent years, measurements performed with electron cyclotron emission imaging (ECEI) have provided insights on the dynamics of this instability prior to and during an ELM crash. ECEI measurements in the KSTAR tokamak[3] show that the ELM evolution can be separated in three different phases. The first is a linear phase where the localized mode grows, the second is a quasi-quiescent state where the mode growth decreases, and the third is when the ELM crash occurs. In the majority of cases, during the linear phase, the rotation of the precursors (structures preceding an ELM crash) is observed in the electron diamagnetic direction. Near the crash, the rotation speed of the precursors decreases and the precursor structure seems to extend radially towards the last closed flux surface where the ELM crash occurs. These measurements are in agreement with AUG ECEI measurements.[4,5] In AUG, the rotation of the ELM precursors is also found in the electron diamagnetic direction but the first-expelled ELM filament is observed to reverse rotation and to propagate in the ion diamagnetic direction. Gas puffing imaging data in NSTX[6] also showed precursors rotating in the electron diamagnetic direction and at the crash, the filament reversing rotation direction (propagating in the ion diamagnetic direction). Recently in JET, fast infra-red thermography measurements at the divertor[7] show ELM precursors stripes moving radially outward. This also suggests ELM precursors structures rotating in the electron diamagnetic direction. In tokamak à configuration variable with magnetic measurements[8] and in MAST using beam emission spectroscopy,[9] similar results were obtained.

Several instabilities can be candidate to explain the ELM precursors. The microtearing mode instability has been proposed as one of the possible candidates.[9,10] This instability shares several characteristics with the experimental measurements, but its radial extend is short (of the order of the ion Larmor radius). This last feature is incompatible with some of the observations. Also, peeling modes and drift waves can be considered, but the firsts are characterized by low toroidal mode numbers that are inconsistent with the observations and the seconds are electrostatic in nature, a characteristic not compatible with the electromagnetic properties of ELM precursors.

Ballooning modes are strong candidates to explain the observations.[11,12] In this manuscript, we will focus on this last instability. Analytically in the linear phase we consider ideal and resistive ballooning modes taking into account bi-fluid diamagnetic effects. Numerical calculations using the nonlinear code JOREK[13,14] are performed. A comparison with the analytical results in the linear stage is carried out. This numerical code is also used to analyze the nonlinear saturation of the instability and to characterize the mechanism that allows to explain the reversal of the filaments rotation at the ELM crash.

II. THE LINEAR BALLOONING MODE ROTATION

The reduced MHD equations over the magnetic flux Ψ, the electric potential Φ, and the pressure P are used to

calculate the dispersion relation associated with the ballooning instability. We use the gyro-viscous cancellation to simplify the equation over Φ (see, e.g., Ref. 15).

The ballooning representation is used to reduce the two-dimensional problem to one dimension (see, e.g., Ref. 16). The following ansatz is applied: $\Phi(\theta,\phi,t)=\sum_{l=-\infty}^{+\infty}\hat{\Phi}(\theta+2\pi l)e^{i(n[\phi-q(\theta+2\pi l)]-\omega t)}$, for a ballooning mode $l=0$, with q being the safety factor, and θ and ϕ are, respectively, the poloidal and toroidal angles. Also, for simplification, we consider the reference frame rotating with the $\boldsymbol{E}\times\boldsymbol{B}$ velocity, hence in this reference frame the equilibrium velocity $\boldsymbol{v}_E=0$ ($\hat{\Phi}_{n=0}=0$, with n being the toroidal mode number). We will add the $\boldsymbol{E}\times\boldsymbol{B}$ velocity contribution at the end of the linear calculation.

Using these hypotheses, the following dispersion relation, in dimensionless form, is found (the details of the derivation are given in the Appendix):

$$\begin{aligned}\omega(\omega-\omega_i^*)&\left[(\omega-\omega_e^*)+\frac{q^2R_0^2(\omega-\omega_e^*+i\eta k_\theta^2)^2}{i\eta k_\theta^2 s^2}\right.\\&\left.\times\left[\omega(\omega-\omega_i^*)+2\gamma_I^2\right]\right]+\gamma_I^2(\omega-\omega_e^*)\\&\times\left(1+\frac{(\omega-\omega_e^*+i\eta k_\theta^2)(2s(1-s)-1)}{2i\eta k_\theta^2 s^2}\right)\\&=\frac{-q^2R_0^2(\omega-\omega_e^*+i\eta k_\theta^2)^2}{i\eta k_\theta^2 s^2}\gamma_I^4,\end{aligned}\tag{1}$$

with the diamagnetic frequencies $\omega_{i/e}^*$ (ion/electron, non-dimensionalized by the Alfvén time τ_A)

$$\omega_i^*=-\omega_e^*=\boldsymbol{v}_i^*\cdot\boldsymbol{e}_\theta\,k_\theta\approx d_i\nabla_r(P_0)k_\theta,\tag{2}$$

the dimensionless diamagnetic velocity $\boldsymbol{v}_i^*=d_i(\boldsymbol{b}\times\nabla P)$, the unit magnetic vector $\boldsymbol{b}$ (this vector is approximated by the toroidal unit vector $\boldsymbol{e}_\phi$), the diamagnetic parameter (or ion inertial length normalized by the major radius) $d_i=(\omega_{Ci}\tau_A)^{-1}=m_i/(eR_0\sqrt{\rho_0\mu_0})$, and the ideal interchange growth rate $\gamma_I=\sqrt{-4\nabla_r(P_0)/(B_0R_0)}$. Also we consider, k_θ is the poloidal wavenumber, P_0 is the axisymmetric pressure, q is the safety factor, s is the magnetic shear, and η is the dimensionless inverse Lundquist number. Finally, B_0, ρ_0, R_0, μ_0, and e are, respectively, a reference magnetic field, density, length, the magnetic permeability, and electric charge.

At high resistivity ($\eta\to\infty$) and strong magnetic shear ($s\gg1$), Eq. (1) simplifies to $\omega(\omega-\omega_i^*)(\omega-\omega_e^*)=(i\gamma_\eta)^3$ with $\gamma_\eta=(k_\theta^2q^2s^{-2}R_0^2\eta\gamma_I^4)^{1/3}$. Considering the diamagnetic frequencies: $\omega_i^*=-\omega_e^*=\omega_*$, the roots of the polynomial can be found using Cardan's method. Taking into account the change of variable: $\omega=i\gamma$, this dispersion relation can be simplified to $\gamma(\gamma^2+\omega_*^2)=\gamma_\eta^3$. Two limits can be identified in this equation, for $\gamma_\eta\gg\omega_*$ the solution $\gamma\approx\gamma_\eta$ and if $\gamma_\eta\ll\omega_*$ we have $\gamma\approx\gamma_\eta^3/\omega_*^2$. In the general case, three roots exist, one real and two complex conjugates.[17] The most unstable root is always the real, and the value of ω is pure imaginary because $\omega=i\gamma$, hence at this limit the unstable mode does not rotate in the considered reference frame.

Also at the ideal limit, $\eta\to0$, and magnetic shear, $s\approx1$, the dispersion relation Eq. (1) simplifies to the second order polynomial[18,19] $\omega^2-\omega_i^*\omega+\gamma_I^2=0$. Two distinct roots exist

$$\omega_\pm=0.5\left(\omega_i^*\pm\sqrt{\omega_i^{*2}-4\gamma_I^2}\right).\tag{3}$$

The system is unstable if $|\omega_i^*/2|<|\gamma_I|$. And the ideal rotation frequency of the mode is $\omega_i^*/2$.[20,21] In this case, the unstable mode rotates at half of the diamagnetic frequency in the ion diamagnetic direction in the considered reference frame.

Moreover, the roots of the general dispersion relation, Eq. (1), can be computed numerically. We find that in realistic cases, i.e., at low resistivity ($\eta<10^{-7}$), the most unstable root is close to the ideal case Eq. (3). In Fig. 1, three computed cases are compared with the analytical solution Eq. (3). One can observe that the imaginary part of the root is close to the ideal theory if the magnetic shear is close to one. With increasing magnetic shear, the calculated mode is more unstable. On the other hand, the real part of the root matches very well the analytical solution. The rotation of the mode, in the reference frame, is almost exactly $\omega_i^*/2$.

To calculate the mode poloidal rotation, in the laboratory reference frame, we add to the intrinsic ballooning mode rotation the equilibrium poloidal $\boldsymbol{E}\times\boldsymbol{B}$ velocity and the equilibrium parallel velocity $V_{//}\cdot b_\theta$ (both velocities projected in the poloidal plane). Hence, the poloidal rotation velocity of the ballooning mode in the laboratory reference frame, in the resistive and ideal limits writes

$$\text{Resistive:}\quad V_{\text{mode}}=V_{\boldsymbol{E}\times\boldsymbol{B}}+V_{//}\cdot b_\theta,\tag{4}$$

$$\text{Ideal:}\quad V_{\text{mode}}=V_{\boldsymbol{E}\times\boldsymbol{B}}+V_{//}\cdot b_\theta+V_i^*/2.\tag{5}$$

The radial electric field in H-mode is observed to be dominated at the pedestal by the radial pressure gradient of the main ions.[22] Also, the pitch angle is considered to be small

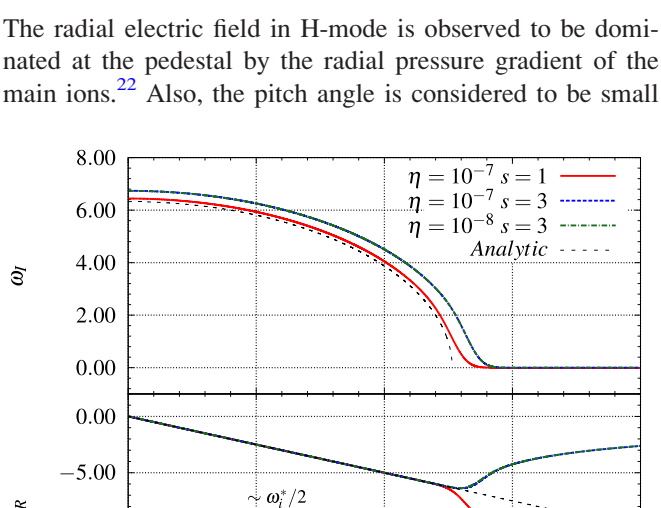

FIG. 1. Evolution of the roots with the diamagnetic frequency ω_i^* (top) imaginary part and (bottom) real part.

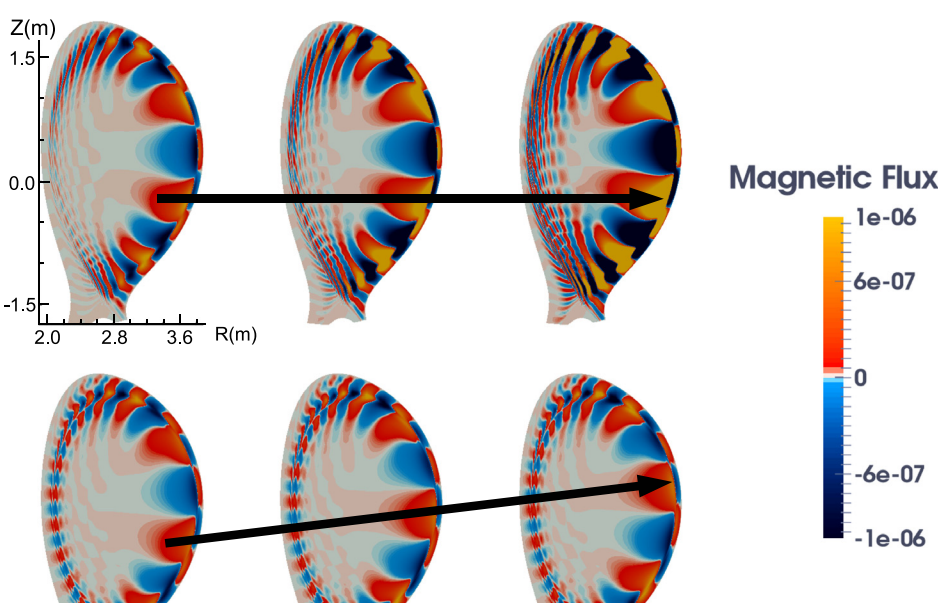

FIG. 2. Magnetic flux perturbation $n=6$, same parameters as in Ref. 25 (10 μs between images) (top) without diamagnetic effects, $d_i=0$ and (bottom) with diamagnetic effects, $d_i = 1.7\times10^{-2}$. In the bottom, the rotation is anticlockwise, i.e., in the electron diamagnetic or $\boldsymbol{E}\times\boldsymbol{B}$ direction.

($\boldsymbol{B}$ is mainly in the toroidal direction ϕ). For these two reasons, in the pedestal region, the poloidal $\boldsymbol{E}\times\boldsymbol{B}$ velocity $V_{\boldsymbol{E}\times\boldsymbol{B}}$ can be approximated by

$$V_{\boldsymbol{E}\times\boldsymbol{B}} = \frac{\boldsymbol{E}\times\boldsymbol{B}}{B^2}\cdot\boldsymbol{e}_\theta \approx \frac{\nabla_r P_i\times\boldsymbol{B}}{enB^2}\cdot\boldsymbol{e}_\theta \approx -\frac{\nabla_r P_i}{enB}, \quad (6)$$

here we use the right handed toroidal coordinate system (r,θ,ϕ). Also, the poloidal ion diamagnetic velocity is approximated by

$$V_i^* = \frac{\boldsymbol{B}\times\nabla P_i}{enB^2}\cdot\boldsymbol{e}_\theta \approx +\frac{\nabla_r P_i}{enB}. \quad (7)$$

In dimensionless units (non-dimensionalized by the Alfvén speed), this velocity becomes

$$V_i^* \approx d_i\nabla_r P_i. \quad (8)$$

Also, the poloidal dimensionless $\boldsymbol{E}\times\boldsymbol{B}$ velocity at the pedestal, where the radial electric field is mostly induced by the radial pressure gradient, writes

$$V_{\boldsymbol{E}\times\boldsymbol{B}} \approx -d_i\nabla_r P_i. \quad (9)$$

The radial gradient of the pressure is negative. Therefore, by convention, we have chosen the $\boldsymbol{E}\times\boldsymbol{B}$ and electron diamagnetic velocities in the positive direction and the ion diamagnetic velocity in the negative direction.

Using the JOREK code,[13,23,24] the linear growth of the ballooning instability with and without diamagnetic effects is analyzed. ELM precursors were previously observed with the JOREK code without diamagnetic effects.[23] Here, we include diamagnetic effects to analyze their effect on the precursors dynamics. The parameters used for the simulations are close to a JET tokamak plasma, as in Ref. 25. Realistic values of the inverse Lundquist number, d_i parameter, and normalized parallel heat conductivity are typically: $\eta = 10^{-8}$, $d_i = 10^{-2}$, and $\kappa_{//} = 10^4$.[26] These values correspond to the following tokamak parameters in JET: $R_0 = 2.9\,\mathrm{m}$, $B_0 = 1.8\,\mathrm{T}$, $n_{ped} = 3.3\times10^{19}\,\mathrm{m}^{-3}$, and $T_{e_{ped}} = T_{i_{ped}} = 1.8\,\mathrm{keV}$.

The magnetic flux perturbation is shown in Fig. 2. Without diamagnetic effects, $d_i=0$, the mode grows and rotates at low speed, as was found in Ref. 13. On the other hand, if diamagnetic effects are taken into account, the mode rotates in the electron diamagnetic direction with a velocity of several km/s. The $\boldsymbol{E}\times\boldsymbol{B}$ velocity is strongly reduced if diamagnetic effects are not taken into account since this velocity is proportional to d_i at the pedestal (see Eq. (9)).

The ballooning mode velocity rotation is plotted against the diamagnetic parameter in Fig. 3. In this figure, we observe a linear scaling with the diamagnetic parameter d_i, in agreement with Eqs. (4)–(9).

In our simulations, the $\boldsymbol{E}\times\boldsymbol{B}$ and the diamagnetic velocities dominate over the poloidally projected parallel velocity ($V_{//}\cdot b_\theta$). Also, we remark that if a field aligned

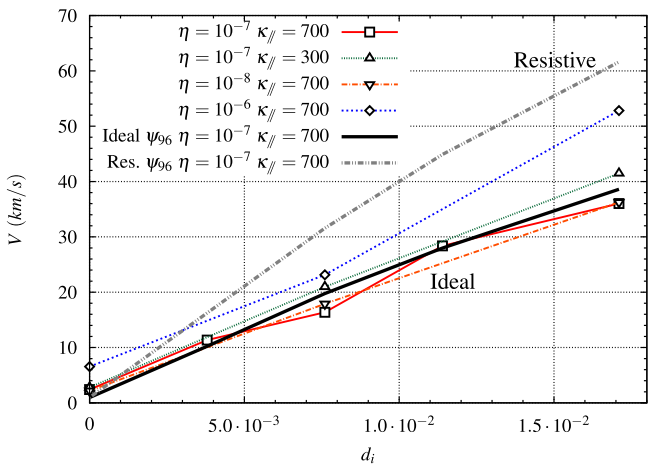

FIG. 3. Poloidal rotation velocity of the modes as a function of d_i and comparison with the expressions Eqs. (4) and (5) taken at Ψ_{96} (i.e., at the flux surface with $|\nabla P|_{max}$), $\kappa_{//}$ is the normalized parallel heat conductivity.

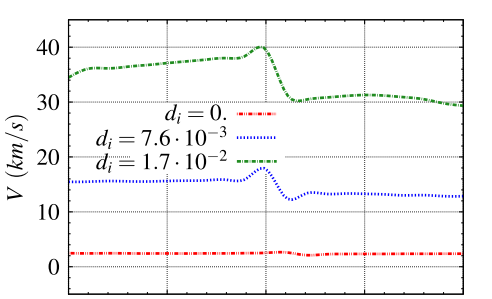

FIG. 4. Poloidal velocity profile of the unstable mode as a function of the normalized magnetic flux (the profiles are averaged at the low field side, $\theta \in [-\pi/2, \pi/2]$).

structure is considered ($k_{//} = 0$), the parallel velocity will not contribute to the apparent poloidal velocity of this structure.

For a small resistivity, the numerical computations are close to the ideal formula Eq. (5) (thick black curve in Fig. 3). We observe that the ballooning mode velocity is always dominated by the $\boldsymbol{E} \times \boldsymbol{B}$ velocity, this mode always rotates in the electron diamagnetic direction. This can be explained as follows: at the pedestal, the ion diamagnetic and $\boldsymbol{E} \times \boldsymbol{B}$ velocities have approximatively the same amplitude but opposite direction (see Eqs. (8) and (9)). For realistic cases (low resistivity), the system behaves close to the ideal limit. At this limit, the ballooning mode rotates with half of the ion diamagnetic velocity (see Eq. (5)). As a consequence, the $\boldsymbol{E} \times \boldsymbol{B}$ velocity is always larger and the ballooning mode rotates in the electron diamagnetic direction in the laboratory reference frame. Therefore, replacing in Eq. (5) the velocities by the expressions given in Eqs. (8) and (9) and neglecting $V_{//} \cdot b_\theta$, the formula estimating the rotation velocity of ELM precursors can be written (in normalized units)

$$V_{mode} \approx -\frac{d_i}{2} \nabla_r P_i, \tag{10}$$

in the electron diamagnetic direction.

During the linear phase, the effect of the $\boldsymbol{E} \times \boldsymbol{B}$ shear on the perturbation is small. We do not observe any deformation of the perturbation in the radial direction (see Fig. 2). The poloidal rotation velocity of the perturbation is almost uniform (see the poloidal velocity profile in Fig. 4). The $\boldsymbol{E} \times \boldsymbol{B}$ shear does not act on the perturbation because the growth rate of the unstable mode is larger that the local $\boldsymbol{E} \times \boldsymbol{B}$ shear rate. In the linear phase, for all the calculations considered: $\omega_{\boldsymbol{E}\times\boldsymbol{B}} < \gamma$. The effect of the $\boldsymbol{E} \times \boldsymbol{B}$ shear becomes important in the nonlinear phase of the instability. In Section III, we will address this nonlinear phase.

III. NONLINEAR DYNAMICS OF ELM FILAMENTS

Experimentally, the rotation of the modes is observed to decrease just before the ELM crash.[3,6] Also, the observations show the rotation of the ELM filaments in the ion diamagnetic direction.[4,6,9] This rotation is opposite to the one observed for the ELM precursors.

With the JOREK code, the nonlinear evolution of the ballooning modes is studied for a case with $d_i = 7.6 \times 10^{-3}$. Near the ELM crash, the density field can be observed in Fig. 5. In this image, filaments of high density are expelled in the ion diamagnetic direction as observed in the experiments.

The inversion of the rotation occurs at the nonlinear saturation of the instability. The perturbed electric potential grows exponentially in the linear phase. It creates periodic vortices with alternating positive and negative rotations. This exponentially growing electric potential saturates when its magnitude is of the same order as the equilibrium electric potential. At this level, the generated $\boldsymbol{E} \times \boldsymbol{B}$ vortices start to interact with the equilibrium density field. The strong correlation between the density and the electric potential can be observed in Fig. 6(a). The $V_{\boldsymbol{E}\times\boldsymbol{B}}$ vortices are deformed, they are thinner in the radial direction and elongated in the poloidal direction, following the magnetic field lines.[27] As observed in Fig. 6(a), the density filament is created and convected by the $\boldsymbol{E} \times \boldsymbol{B}$ velocity vortex. Also, from the density ρ equation, we can show that the density motion is governed by the $\boldsymbol{E} \times \boldsymbol{B}$ velocity term, this equation writes

$$\partial_t \rho = 1/R[\rho R^2, \Phi] + d_i\, \partial_Z P + \text{Diff.} + \text{Source}, \tag{11}$$

with the Poisson bracket defined as: $[f, g] = \boldsymbol{e}_\phi \cdot (\nabla f \times \nabla g)$ —in cylindrical coordinates, (R, Z, ϕ)— (the Poisson bracket term corresponds to the $\boldsymbol{E} \times \boldsymbol{B}$ convection term: $-\boldsymbol{v}_E \cdot \nabla \rho$). In this equation, the diamagnetic velocity (second term on the right hand side) does not act as an advection term but only as a compression term. Therefore, only the $\boldsymbol{E} \times \boldsymbol{B}$ velocity convects the density filament (first term on the right hand side).

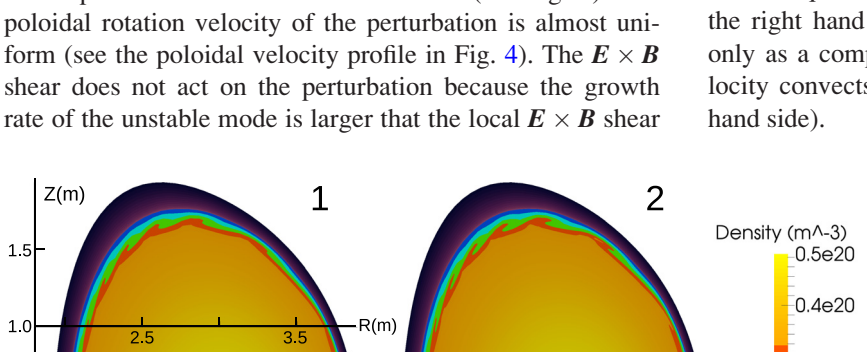

FIG. 5. Density filaments are expelled in ion diamagnetic direction, $d_i = 7.6 \times 10^{-3}$ (5 μs between images).

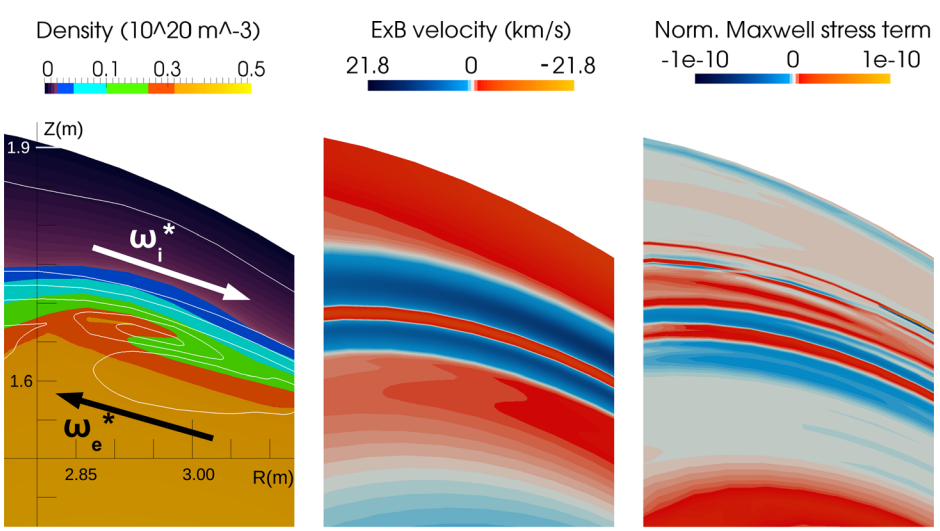

FIG. 6. (a) Density filament (colormap) and electric potential isocontours (white lines), (b) axisymmetric $\boldsymbol{E}\times\boldsymbol{B}$ velocity, and (c) normalized Maxwell stress term $R^{-1}[\Psi,j]$. All these quantities are taken at the same instant, during the ELM crash ($t=1273\,\mu$s in Figs. 7 and 8).

The profiles of the axisymmetric component of the $\boldsymbol{E}\times\boldsymbol{B}$ velocity are plotted in Fig. 7 as a function of the normalized magnetic flux. In this figure, we observe a strong velocity shear created during the ELM crash (see also Fig. 6(b)). At the same time as the filament is convected, a strong $\boldsymbol{E}\times\boldsymbol{B}$ shear appears. In the region where the mode perturbation is larger ($\Psi_N\approx 0.96$), the velocity profile decreases and crosses the zero abscissa axis. This can explain why experimentally the ELM precursors decelerate approaching the crash. The shear increases further and the $\boldsymbol{E}\times\boldsymbol{B}$ velocity becomes negative. This effect makes the high density filament to cut from the main plasma, and the filament is expelled.

The different terms of the $\boldsymbol{E}\times\boldsymbol{B}$ vorticity w_E equation, implemented in the JOREK code, are plotted as a function of time in Fig. 8 (averaged on the closed flux surface region for $n=0$). The vorticity equation is the projection, in the toroidal direction, of the curl of the momentum equation. This equation writes

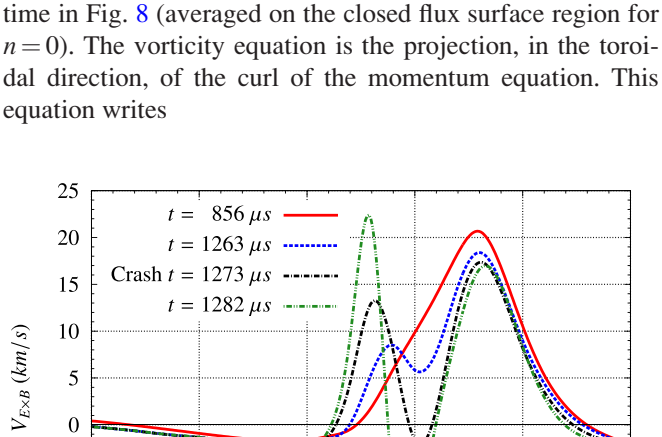

FIG. 7. Axisymmetric ($n=0$) $\boldsymbol{E}\times\boldsymbol{B}$ velocity profiles during an ELM crash (averaged in the region between the low field side and the vertical direction $\theta\in[0,\pi/2]$).

$$\nabla\phi\cdot\nabla\times\{R^2[\rho\partial_t\boldsymbol{v}_E=-\rho(\boldsymbol{v}_E\cdot\nabla)\boldsymbol{v}_E-\rho(\boldsymbol{v}_i^*\cdot\nabla)\boldsymbol{v}_E-\nabla P+\boldsymbol{j}\times\boldsymbol{B}+\mu\nabla^2\boldsymbol{v}_E]\},\tag{12}$$

with $\nabla\phi=1/R\,\boldsymbol{e}_\phi$, ϕ being the toroidal direction, and μ being the dynamic viscosity. The weak form of this equation allows to integrate the different terms in a volume. In weak form, the expression of the vorticity equation is

$$\begin{aligned}\delta_t w_E &= -\int\hat{\rho}\nabla u^*\cdot\nabla_\perp(\delta_t\Phi)dV\\ &=\int\Big(-\frac{v_E^2}{2R}[u^*,\hat{\rho}]-R\hat{\rho}\,w_E[u^*,\Phi]+R[u^*,P]\\ &\quad -u^*\nabla\phi\cdot\nabla\times\Big(R^2\rho\big(\boldsymbol{v}_i^*\cdot\nabla\big)\boldsymbol{v}_E\Big)+u^*\frac{1}{R}[\Psi,j]\\ &\quad -u^*\frac{F_0}{R^2}\partial_\phi j+u^*\nabla\phi\cdot\nabla\times\big(R^2\mu\nabla^2\boldsymbol{v}_E\big)\Big)dV,\end{aligned}\tag{13}$$

with u^* being a test function and $\hat{\rho}=R^2\rho$. The first two terms on the right hand side correspond to the term $-\rho(\boldsymbol{v}_E\cdot\nabla)\boldsymbol{v}_E$ in the momentum equation. The third term on the right hand side is the pressure term, and the fourth corresponds to the diamagnetic velocity term *Dia*. The fifth and sixth terms correspond to the $\boldsymbol{j}\times\boldsymbol{B}$ term in the momentum equation, and the last term is the viscosity term *Visco*. For more details, we refer to Refs. 13, 23, 24, and 26.

In Fig. 8, the equilibrium noted *Eq* is the static equilibrium: pressure $R[u^*,P]$ plus Maxwell stress tensor $R^{-1}[\Psi,j]$ (in strong form: $Eq=\nabla\phi\cdot\nabla\times\{R^2\,[\boldsymbol{j}\times\boldsymbol{B}-\nabla P\,]\}$). In the linear phase $t\le 1.23$ ms, we find $Eq+Visco\approx 0$, and the Maxwell stress term is balanced by the pressure and by the viscous dissipation of the equilibrium flows. A description of these flows can be found in Ref. 28. At $t\approx 1.24$ ms, in Fig. 8, the diamagnetic term $-\nabla\phi\cdot\nabla\times(R^2\rho(\boldsymbol{v}_i^*\cdot\nabla)\boldsymbol{v}_E)$ (*Dia*) grows but is still balanced by the equilibrium *Eq* and the viscosity term. Then, at $t=1.273$ ms (same time as in Fig. 6), the ELM crash occurs. The term $\delta_t w_E$ becomes large, and strong axisymmetric ($n=0$) vorticity is created. This

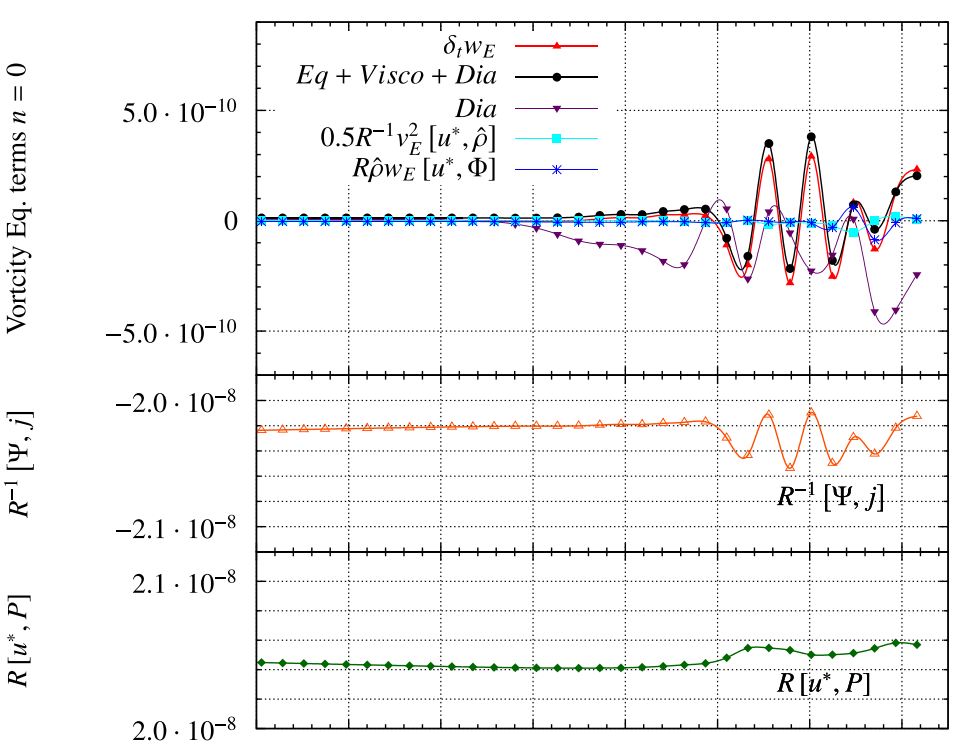

FIG. 8. Axisymmetric (toroidal mode number $n=0$) $\boldsymbol{E}\times\boldsymbol{B}$ vorticity equation terms (see Eq. (12)) as a function of time.

vorticity is generated nonlinearly by the unbalance between the terms in the vorticity equation. The terms dominating the w_E dynamics are the Maxwell stress tensor $R^{-1}[\Psi,j]$[13] (see also Fig. 6(c)) and the *Dia* term.

The two larger terms in the vorticity equation are the Maxwell stress tensor and the pressure terms (see Fig. 8, center and bottom). At the nonlinear crash, the larger term governing the vorticity evolution is $R^{-1}[\Psi,j]$. The pressure term $R[u^*,P]$ is of the same order of magnitude (with opposite sign), but it does not behave with the same dynamic as the time derivative of the vorticity $\delta_t w_E$. This behavior suggests that magnetic activity is enhanced at the nonlinear phase. Magnetic reconnection seems to play an important role at the ELM crash; this phenomenon was suggested in Ref. 29 and recently in Ref. 30. The detailed study of the magnetic reconnection at the ELM crash will be left for a future work.

IV. CONCLUSION

The behavior of the linear ballooning instability is close to the ideal limit if realistic values of the tokamak plasma resistivity are considered. The ideal ballooning calculation yields a formula, Eq. (10), that estimates the rotation velocity of ELM precursors. This linear analysis is confirmed by JOREK simulations and explains the ELM precursors rotation observed experimentally. This rotation is in the electron diamagnetic direction and is found to increase linearly with d_i (the ion inertial length normalized by the major radius of the tokamak). In the linear phase, the $\boldsymbol{E}\times\boldsymbol{B}$ shear rate is smaller than the growth rate of the ballooning instability. Therefore, the $\boldsymbol{E}\times\boldsymbol{B}$ shear does not interact with the perturbation and the unstable mode is observed to rotate with a uniform velocity in the poloidal direction.

The electric potential perturbation grows exponentially in the linear phase. At the nonlinear saturation, its amplitude is of the same order as the electric potential equilibrium field. Consequently, it convects the density field and forms filaments of density. At the same time, the perturbation interacts nonlinearly and creates an axisymmetric $\boldsymbol{E}\times\boldsymbol{B}$ velocity shear. This strong shear leads to the expulsion of the density filaments outside the main plasma. This moment corresponds to the ELM crash. The generated axisymmetric flow leads to the reversal of the filaments rotation. The rotation is in the ion diamagnetic direction, as observed experimentally. Looking at the terms in the vorticity equation, we observe that the one dominating the nonlinear generation of flows is the Maxwell stress tensor. This behavior indicates that magnetic reconnection occurs inside the plasma, leading to a more complex dynamical picture.

An interesting perspective for the present work is the study of the magnetic reconnection at the ELM crash. The transport, parallel to the magnetic field lines, is very fast (of the order of the ion sound speed in the scrape-off layer). Therefore, the changes in the magnetic topology at the plasma edge can connect a core region, with high density and temperature, with the scrape-off layer region. This could considerably modify the power deposition on the plasma-facing components of a tokamak.

ACKNOWLEDGMENTS

This project has been carried out within the framework of the EUROfusion Consortium and has received funding from the Euratom research and training program 2014–2018 under Grant Agreement No. 633053. This work has benefited from financial support from the French National Research

Agency (ANR): ANEMOS (2011). A part of this work was carried out using the CCRT-CURIE supercomputer within project GENCI (gen2197) and PRACE (ra1904) and the HELIOS super-computer system (IFERC-CSC). The views and opinions expressed herein do not necessarily reflect those of the European Commission or the ITER Organization.

APPENDIX: DERIVATION OF THE BALLOONING DISPERSION RELATION

The ballooning dispersion relation is derived from: the induction, the vorticity, and the pressure equations. In dimensionless form, the induction equation writes

$$\partial_t \Psi + d_i \nabla_{//} P - \nabla_{//} \Phi = \eta \Delta \Psi, \tag{A1}$$

with $P = P_i = P_e$ being the pressure, Ψ being the magnetic flux function, and Φ being the electric potential. The dimensionless vorticity equation (with the gyro-viscous cancellation[15]) yields

$$-[\partial_t + (\boldsymbol{v}_E + \boldsymbol{v}_i^*)\cdot\nabla]\nabla_\perp^2 \Phi - 2\boldsymbol{g}\cdot\nabla P + \nabla_{//}(\Delta\Psi) = 0, \tag{A2}$$

with the vector

$$\boldsymbol{g} = -\frac{2}{B}\left(\frac{\boldsymbol{B}}{B}\times\frac{\nabla B}{B}\right). \tag{A3}$$

The dimensionless pressure equation, considering the media incompressible, is

$$\partial_t P + \boldsymbol{v}_E\cdot\nabla P = 0. \tag{A4}$$

In these equations, we have taken into account Ampère's Law (we consider the current density in the toroidal direction)

$$j_\phi = \frac{1}{\mu_0}\Delta\Psi. \tag{A5}$$

To simplify these equations, we take into account the reference frame rotating with the $\boldsymbol{E}\times\boldsymbol{B}$ velocity, hence in this reference frame the equilibrium speed $\boldsymbol{v}_E|_{n=0} = 0$. For simplicity, we set the equilibrium electric potential to zero ($\Phi|_{n=0} = 0$). In the vorticity equation, we also neglect the advection by the perturbation (this is a second order term) and Eq. (A2) becomes

$$-[\partial_t + \boldsymbol{v}_i^*\cdot\nabla]\nabla_\perp^2\tilde{\Phi} - 2\boldsymbol{g}\cdot\nabla P + \nabla_{//}(\Delta\Psi) = 0, \tag{A6}$$

with $\tilde{\Phi}$ being the electric potential perturbation. The dimensionless diamagnetic velocity is expressed as

$$\boldsymbol{v}_i^* = d_i(\boldsymbol{b}\times\nabla P). \tag{A7}$$

Using the ballooning representation, an eikonal form is retained for the perturbation of the three scalar fields (Ψ, Φ, and P). Explicitly, for the electric potential, we have

$$\tilde{\Phi}(r,\theta,\varphi,t) = \hat{\Phi}(\theta)e^{i[n(\varphi - q(r)\theta) - \omega t]}. \tag{A8}$$

In Fourier space, the $\boldsymbol{k}\cdot\boldsymbol{g}$ term appearing in Eq. (A6) can be written as

$$\boldsymbol{k}\cdot\boldsymbol{g} = \frac{2}{B_0 R_0}\left[k_\theta\cos(\theta) + k_r\sin(\theta)\right]. \tag{A9}$$

From Eq. (A8), we can derive the following relations:

$$\begin{aligned} &k_\theta = -\frac{nq}{r}, \quad k_r = -\frac{nqs\theta}{r}, \quad \frac{k_r}{k_\theta} = s\theta,\\ &k_\perp^2 = k_\theta^2[1 + s^2\theta^2],\\ &k_{//} = -\frac{i}{qR_0}\partial_\theta, \end{aligned} \tag{A10}$$

with

$$s = \frac{r}{q}\frac{dq}{dr}. \tag{A11}$$

Using Eqs. (A8)–(A10), we linearize and combine Eqs. (A1), (A4), and (A6). The following equation is derived:

$$\begin{aligned} &\frac{(\omega - \omega_e^*)k_\perp^2}{(\omega - \omega_e^* + i\eta k_\perp^2)}\frac{1}{q^2R_0^2}\partial_{\theta\theta}\hat{\Phi} + \omega(\omega - \omega_i^*)k_\perp^2\hat{\Phi}\\ &\quad + \gamma_I^2 k_\theta^2[\cos(\theta) + s\theta\sin(\theta)]\hat{\Phi} = 0. \end{aligned} \tag{A12}$$

This last equation can be expressed in the form

$$-\partial_{\theta\theta}\hat{\Phi} + G(\theta)\hat{\Phi} = 0. \tag{A13}$$

Performing a Taylor expansion of the G function around $\theta = 0$ (where the amplitude of the ballooning mode is maximum). We can use a second order polynomial that approximates the function $G(\theta)|_{\theta=0}$. This approximation writes

$$-\partial_{\theta\theta}\hat{\Phi} + (a(\omega)\theta^2 + b(\omega))\hat{\Phi} = 0. \tag{A14}$$

In this form, the equation has the following particular solution (see, e.g., the harmonic oscillator in quantum mechanics, page 124 in Ref. 31):

$$\hat{\Phi}(\theta) = \hat{\Phi}_0 e^{-\alpha\frac{\theta^2}{2}}. \tag{A15}$$

The polynomial coefficients $a(\omega)$ and $b(\omega)$ can be expressed as

$$a(\omega) = \alpha^2 \quad \text{and} \quad b(\omega) = -\alpha. \tag{A16}$$

From these relations, the dispersion relation can be obtained using the following equality:

$$a(\omega) = b^2(\omega). \tag{A17}$$

The one dimensional dispersion relation yields

$$\begin{aligned} &(\omega - \omega_e^*)\left(i\eta k_\theta^2 s^2[\omega(\omega - \omega_i^*) + \gamma_I^2]\right.\\ &\quad\left. + \frac{\gamma_I^2}{2}(\omega - \omega_e^* + i\eta k_\theta^2)(2s(1-s) - 1)\right)\\ &\quad = -q^2R_0^2(\omega - \omega_e^* + i\eta k_\theta^2)^2[\omega(\omega - \omega_i^*) + \gamma_I^2]^2. \end{aligned} \tag{A18}$$

This relation can be written as Eq. (1).

[1]A. Leonard, Phys. Plasmas **21**, 090501 (2014).
[2]G. Huijsmans, C. Chang, N. Ferraro, L. Sugiyama, F. Waelbroeck, X. Xu, A. Loarte, and S. Futatani, Phys. Plasmas **22**, 021805 (2015).
[3]G. Yun, W. Lee, M. Choi, J. Lee, H. Park, B. Tobias, C. Domier, N. Luhmann, Jr., A. Donné, J. Lee *et al.*, Phys. Rev. Lett. **107**, 045004 (2011).

[4]J. Boom, I. Classen, P. De Vries, T. Eich, E. Wolfrum, W. Suttrop, R. Wenninger, A. Donné, B. Tobias, C. Domier *et al.*, Nucl. Fusion **51**, 103039 (2011).
[5]I. Classen, J. Boom, A. Bogomolov, E. Wolfrum, M. Maraschek, W. Suttrop, P. de Vries, A. Donné, B. Tobias, C. Domier *et al.*, Nucl. Fusion **53**, 073005 (2013).
[6]Y. Sechrest, T. Munsat, D. Battaglia, and S. Zweben, Nucl. Fusion **52**, 123009 (2012).
[7]M. Rack, B. Sieglin, J. Pearson, T. Eich, Y. Liang, P. Denner, A. Wingen, L. Zeng, I. Balboa, S. Jachmich *et al.*, Nucl. Fusion **54**, 064012 (2014).
[8]R. Wenninger, H. Reimerdes, O. Sauter, and H. Zohm, Nucl. Fusion **53**, 113004 (2013).
[9]A. Kirk, D. Dunai, M. Dunne, G. Huijsmans, S. Pamela, M. Bécoulet, J. Harrison, J. Hillesheim, C. Roach, and S. Saarelma, Nucl. Fusion **54**, 114012 (2014).
[10]P. Manz, J. Boom, E. Wolfrum, G. Birkenmeier, I. Classen, N. Luhmann, Jr., U. Stroth *et al.*, Plasma Phys. Controlled Fusion **56**, 035010 (2014).
[11]P. Snyder, H. Wilson, J. Ferron, L. Lao, A. Leonard, T. Osborne, A. Turnbull, D. Mossessian, M. Murakami, and X. Xu, Phys. Plasmas **9**, 2037 (2002).
[12]A. J. Webster, Nucl. Fusion **52**, 114023 (2012).
[13]G. Huysmans and O. Czarny, Nucl. Fusion **47**, 659 (2007).
[14]O. Czarny and G. Huysmans, J. Comput. Phys. **227**, 7423 (2008).
[15]D. Schnack, D. Barnes, D. Brennan, C. Hegna, E. Held, C. Kim, S. Kruger, A. Pankin, and C. Sovinec, Phys. Plasmas **13**, 058103 (2006).
[16]J. Connor, R. Hastie, and J. Taylor, in *Proceedings of the Royal Society of London A: Mathematical, Physical and Engineering Sciences* (The Royal Society, 1979), Vol. 365, pp. 1–17.
[17]P. Diamond, P. Similon, T. Hender, and B. Carreras, Phys. Fluids **28**, 1116 (1985).
[18]K. Roberts and J. Taylor, Phys. Rev. Lett. **8**, 197 (1962).
[19]W. Tang, R. L. Dewar, and J. Manickam, Nucl. Fusion **22**, 1079 (1982).
[20]G. Huysmans, S. Sharapov, A. Mikhailovskii, and W. Kerner, Phys. Plasmas **8**, 4292 (2001).
[21]G. Huysmans, Plasma Phys. Controlled Fusion **47**, B165 (2005).
[22]E. Viezzer, T. Pütterich, G. Conway, R. Dux, T. Happel, J. Fuchs, R. McDermott, F. Ryter, B. Sieglin, W. Suttrop *et al.*, Nucl. Fusion **53**, 053005 (2013).
[23]S. Pamela, G. Huysmans, M. Beurskens, S. Devaux, T. Eich, S. Benkadda *et al.*, Plasma Phys. Controlled Fusion **53**, 054014 (2011).
[24]F. Orain, M. Bécoulet, G. Dif-Pradalier, G. Huijsmans, S. Pamela, E. Nardon, C. Passeron, G. Latu, V. Grandgirard, A. Fil *et al.*, Phys. Plasmas **20**, 102510 (2013).
[25]M. Bécoulet, F. Orain, G. Huijsmans, S. Pamela, P. Cahyna, M. Hoelzl, X. Garbet, E. Franck *et al.*, Phys. Rev. Lett. **113**, 115001 (2014).
[26]A. Fil, E. Nardon, M. Hoelzl, G. T. A. Huijsmans, F. Orain, M. Becoulet, P. Beyer, G. Dif-Pradalier, R. Guirlet *et al.*, Phys. Plasmas **22**, 062509 (2015).
[27]N. Fedorczak, P. Diamond, G. Tynan, and P. Manz, Nucl. Fusion **52**, 103013 (2012).
[28]S. Pamela, G. Huysmans, and S. Benkadda, Plasma Phys. Controlled Fusion **52**, 075006 (2010).
[29]R. Fitzpatrick, Phys. Plasmas **1**, 3308 (1994).
[30]T. Rhee, S. S. Kim, H. Jhang, G. Y. Park, and R. Singh, Nucl. Fusion **55**, 032004 (2015).
[31]A. Phillips, *Introduction to Quantum Mechanics* (John Wiley & Sons, 2003).